6-28-2022

Vortex Sheet Sensitivity to Low-Level Vertical Shear and Airmass Temperature Perturbation

Adam L. Houston

George L. Limpert

Vortex Sheet Sensitivity to Low-Level Vertical Shear and Airmass Temperature Perturbation

ADAM L. HOUSTON[a] AND GEORGE LIMPERT[a]

[a] *Department of Earth and Atmospheric Sciences, University of Nebraska–Lincoln, Lincoln, Nebraska*

(Manuscript received 21 September 2021, in final form 28 June 2022)

ABSTRACT: A theoretical, numerical-modeling-based examination of the sensitivity of vortex sheets along airmass boundaries to the following three characteristics is presented: 1) boundary-normal component of the vertical wind shear, 2) boundary-parallel component of the vertical wind shear, and 3) temperature perturbation within the parent air mass of the boundary. The overall aim of this work is to advance understanding of the sensitivity of micro-α- to meso-γ-scale vortex generation along airmass boundaries to the ambient environment. Density currents are simulated in a 2D domain that does not allow baroclinic generation of near-surface vertical vorticity (ζ_{ns}) with parameterized latent heating for convection initiated at the associated airmass boundary and Coriolis turned on. Despite the absence of baroclinically generated ζ_{ns}, with Coriolis turned on and without any boundary-parallel shear, ζ_{ns} more than two orders of magnitude larger than planetary vorticity is generated along the boundary and located within the cold air. The magnitude of ζ_{ns} is found to increase with increasing boundary-normal shear with statistically significant intra-experiment separations. Near-surface vertical vorticity ζ_{ns} is found to scale inversely with boundary-parallel shear with a transition to negative leading-edge ζ_{ns} in several of the larger boundary-normal shear simulations. An inverse and statistically significant relationship is found between ζ_{ns} and the temperature perturbation within the parent air mass of the boundary ($\Delta\theta$), and is a direct consequence of the dependence of boundary propagation speed on $\Delta\theta$.

SIGNIFICANCE STATEMENT: Research presented in this article aims to contribute to an improved understanding of the environmental controls on the generation of small-scale vortices along airmass boundaries. Vertical shear, both along and across an airmass boundary, as well as temperature of the air mass on the cool side of an airmass boundary are found to regulate the magnitude of near-surface vertical vorticity available to small-scale vortices.

KEYWORDS: Density currents; Mesoscale processes; Mesoscale systems

1. Introduction

The aim of this work is to contribute to an improved understanding of the sensitivity of micro-α- to meso-γ-scale vortices (e.g., tornadoes, mesovortices, and misocyclones) along airmass boundaries to low-level vertical shear and temperature perturbation within the boundary's parent air mass. We aim to expose potential sensitivities through idealized numerical simulations of 2D vortex sheets. Micro-α- to meso-γ-scale vortices usually emerge from vortex sheets in place along airmass boundaries. However, important differences concerning the source of rotation for tornadoes, mesovortices, and misocyclones make it challenging for any single study to offer broad guidance on the environmental and storm-scale controls on micro-α- to meso-γ-scale vortex genesis and strength. Moreover, the 2D frame of reference adopted for this work cannot simulate vortices that might ultimately develop from vortex sheets. Nevertheless, the sensitivity of vortex sheet magnitude to the ambient state could reveal important environmental conditions required for micro-α- to meso-γ-scale vortex formation.

Analysis presented herein focuses on the theoretical impact of the following three characteristics on 2D near-surface vertical vorticity (ζ_{ns}): 1) boundary-normal component of the vertical wind shear, 2) boundary-parallel component of the vertical wind shear, and 3) temperature perturbation within the parent air mass of the boundary. Vertical shear contributes directly to the vertical vorticity of near-surface vortices when (barotropic) horizontal vorticity associated with the vertical shear is reoriented into the vertical in descending air (Walko 1993; Davies-Jones et al. 2001; Markowski et al. 2008). This process would ostensibly manifest as u-shaped vortex lines (Markowski et al. 2008; Davies-Jones 2015). The contribution to horizontal vorticity from baroclinic effects is likely to be significant (Davies-Jones and Brooks 1993; Trapp and Weisman 2003; Atkins and St. Laurent 2009; Dahl et al. 2014; Markowski et al. 2014). Thus, to identify the direct contribution to ζ_{ns} from the vertical shear it is necessary to isolate the barotropic component of the horizontal vorticity. This can be achieved through decomposition of vorticity along trajectories passing into the vortex (e.g., Dahl et al. 2014) or through numerical experiments with a symmetric dimension orthogonal to density gradients (e.g., Davies-Jones 2000; Houston 2016), which removes the relevant baroclinic component.

Vertical shear can also contribute *indirectly* to ζ_{ns} along airmass boundaries. The source of near-surface rotation would not originate in the horizontal vorticity of the vertical shear but, instead, the role of vertical shear would be to alter the strength and/or distribution of vertical motion so as to facilitate stretching of existing ζ_{ns} (Markowski and Richardson 2014). Above-ground fluid rotation near the parent airmass

Corresponding author: Adam L. Houston, ahouston2@unl.edu

DOI: 10.1175/MWR-D-21-0249.1

TABLE 1. Free parameters used for the full experiment set.

$\Delta\theta$	Max potential temperature deficit within cold block (K)	2, 4, 6, 8, 10, 12
J_0	Max value of diabatic heating within deep convection (K s^{-1})	0.0, 0.06, 0.12
$d\bar{u}/dz$	Boundary-normal low-level vertical shear (s^{-1})	0.0, 0.002, 0.004, 0.006, 0.008, 0.010, 0.012, 0.014
$d\bar{v}/dz$	Boundary-parallel low-level vertical shear (s^{-1})	0.0, 0.002, 0.004, 0.006, 0.008, 0.010, 0.012, 0.014

boundary can result in a vertical pressure gradient force (VPGF) that gives rise to this vertical motion. Specifically, an above-ground reduction in pressure could be generated in a localized region of ζ (e.g., a mesocyclone) as a consequence of the tilting of horizontal vorticity associated with the vertical shear by a deep convective updraft (Rotunno and Klemp 1982; Davies-Jones 1984; Markowski and Richardson 2014). Above-ground pressure reductions can also result from horizontal vorticity along the sloped leading edge of the dense air mass associated with the airmass boundary (Houston 2016); a mechanism controlled in part by the boundary-normal component of the vertical shear (Houston 2016). Boundary-parallel gradients in boundary-normal shear associated with boundary waviness could also enhance tilting of horizontal vorticity which could increase above-ground ζ and, as reviewed above, increase stretching of existing ζ_{ns} (Houston 2016, 2017).

Boundary propagation speed should also theoretically regulate the VPGF *ahead of* the boundary through the fluid extension term: positive (stagnation) pressure perturbations near the surface ahead of the boundary should scale directly with convergence and thus directly with boundary propagation speed (Houston 2016). Since, boundary-normal vertical shear alters boundary propagation speed (Xu 1992), upward motion ahead of the boundary should theoretically scale with the boundary-normal vertical shear (Xue et al. 1997; Bryan and Rotunno 2014; Houston 2016). This would result in stretching of existing ζ_{ns} ahead of the boundary.

Boundary-normal vertical shear will also alter the phasing of an airmass boundary and the surmounting deep convection (Rotunno et al. 1988; Fovell and Ogura 1989) which will alter the spatial relationship between the VPGF, associated with both the in-cloud positive buoyancy and subcloud ζ, with ζ_{ns} along the boundary (Brooks et al. 1994; Houston 2016). This relationship between vertical shear and phasing is partly due to the impact of vertical shear on boundary propagation speed but also due to the impact of vertical shear on the speed of the cloud-bearing flow (Fovell and Ogura 1989; Fovell and Dailey 1995).

Ultimately, the theoretical impact of vertical shear on the strength of near-surface vortex sheets along airmass boundaries can be categorized as follows:

- Direct: horizontal vorticity of the vertical shear is the source of rotation
- Indirect 1: Vertical shear contributes to above-surface ζ that ultimately results in stretching of existing ζ_{ns}.
- Indirect 2: Vertical shear alters boundary propagation speed and associated above-surface horizontal vorticity that ultimately results in stretching of ζ_{ns} behind the boundary.
- Indirect 3: Vertical shear alters boundary propagation speed and associated near-surface convergence and stretching of ζ_{ns} *ahead of* the boundary.
- Indirect 4: Vertical shear alters the phasing of above-surface VPGF with ζ_{ns} thereby regulating the stretching of ζ_{ns}.

The temperature perturbation within the parent air mass of the boundary could theoretically impact the generation of ζ_{ns}

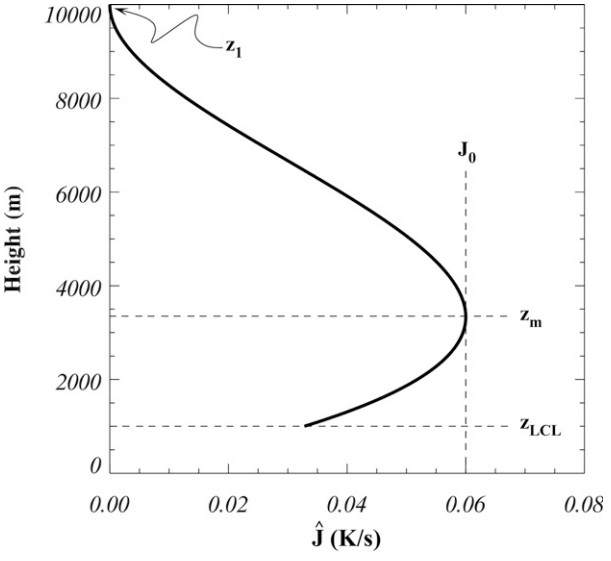

FIG. 1. Vertical profile of $\hat{J}$ for $J_0 = 0.06$ K s^{-1}.

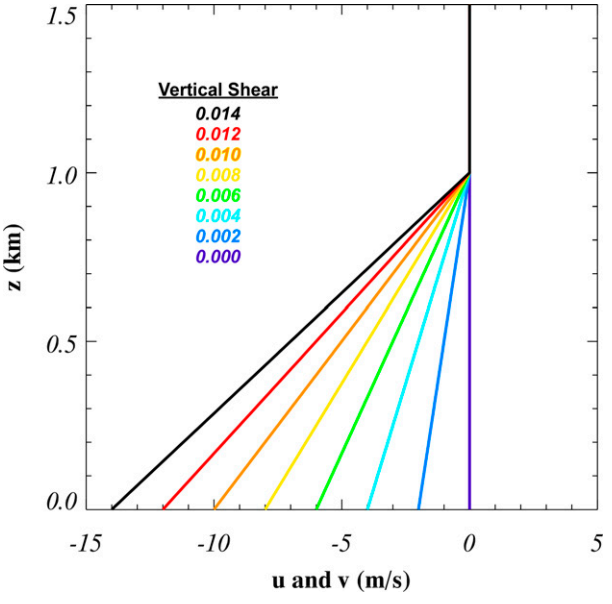

FIG. 2. Vertical profiles of both $\bar{u}$ and $\bar{v}$ for the values of vertical shear used in the experiments conducted for this work.

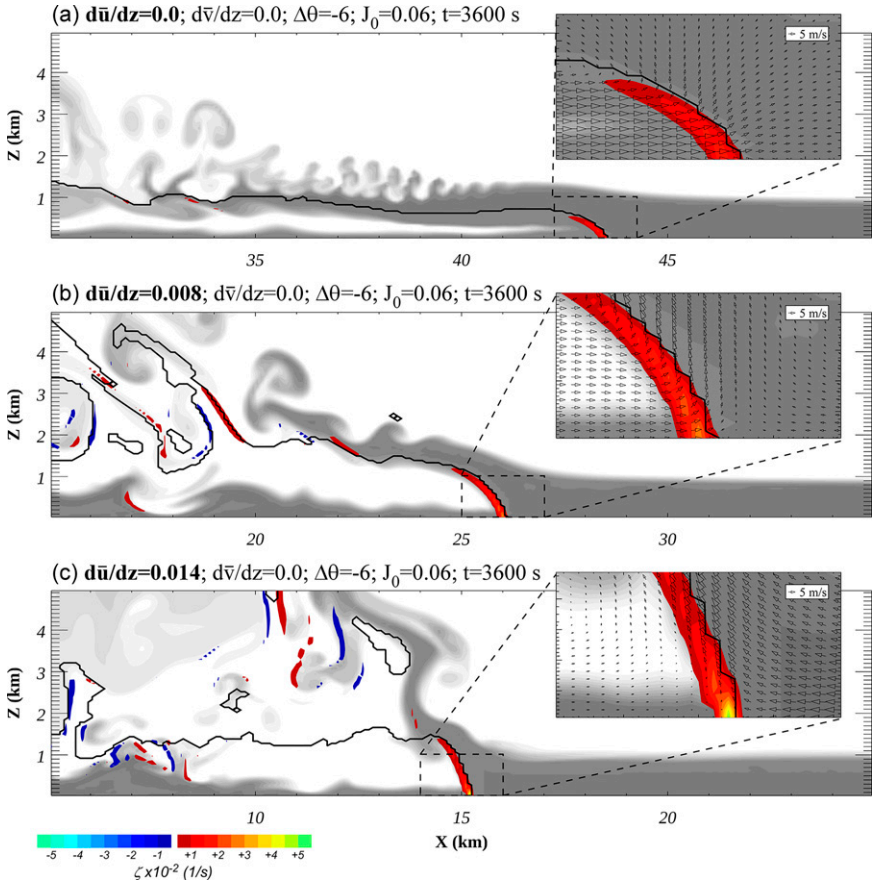

FIG. 3. Vertical vorticity (shaded in color), tracer concentration (shaded in grayscale), and $\theta' = -1$ K at 3600 s for the simulations with $d\bar{v}/dz = 0\,\mathrm{s}^{-1}$, $\Delta\theta = -6$ K, $J_0 = 0.06$ K s^{-1}, and (a) $d\bar{u}/dz = 0\,\mathrm{s}^{-1}$, (b) $d\bar{u}/dz = 0.008\,\mathrm{s}^{-1}$, and (c) $d\bar{u}/dz = 0.014\,\mathrm{s}^{-1}$. Inset panels also show u–w wind vectors. Because the surface wind speed scales directly with $d\bar{u}/dz$ (refer to Fig. 2), the domain-relative forward propagation of the density current decreases with increasing $d\bar{u}/dz$.

through associated static stability which could suppress vertical motion and associated stretching and tilting (Markowski and Richardson 2014). However, temperature perturbation will also regulate boundary propagation speed which has been shown to increase the ascent within the cold air near the boundary (Houston 2016). Because of the role that temperature might play in regulating the vertical motion within the cold air, temperature in the parent air mass of the boundary might also alter the sensitivity of ζ_{ns} to vertical shear particularly for effects that require vertical motion within the dense air mass.

Positive buoyancy in surmounting deep convection can alter the magnitude of the buoyant VPGF and therefore the degree to which phasing of above-surface VPGF with ζ_{ns} amplifies existing ζ_{ns} through stretching ("Indirect 4"). Larger positive buoyancy (even in the absence of precipitation) could also promote more significant subcloud overturning and mixing within the parent air mass for the boundary.

Numerical modeling-based experiments are used for this work to isolate the impact of environmental characteristics on ζ_{ns} along airmass boundaries. Slab symmetry (2D framework) is used to reduce the categories of mechanisms that can contribute to ζ_{ns}. Specifically, this experiment design prevents the direct contribution from the boundary-normal component of the vertical shear (e.g., Houston 2016). It also prevents the indirect contribution from above-surface ζ ("Indirect 1") since 2D ζ exhibits no curvature and thus cannot produce a pressure deficit. Finally, it removes the contribution from the phasing of subcloud ζ with ζ_{ns} ("Indirect 4") since, as just noted, in the absence of curvature, there is no VPGF associated with ζ; the contribution from "Indirect 4" through the VPGF associated with in-cloud buoyancy remains.

Overall, the reduction in complexity afforded by imposing slab symmetry means that these results have limited direct applicability to the generation of supercell tornadoes. Furthermore, these results cannot be used to address the relative contribution to ζ_{ns} from baroclinic versus barotropic sources of vorticity since density gradients are orthogonal to the symmetric dimension and thus baroclinically generated horizontal vorticity cannot contribute to ζ_{ns}. These results also cannot be used to evaluate the potential importance of barotropic instability on vortex generation (e.g., Lee and Wilhelmson 1997; Wheatley and Trapp 2008). However, these results can

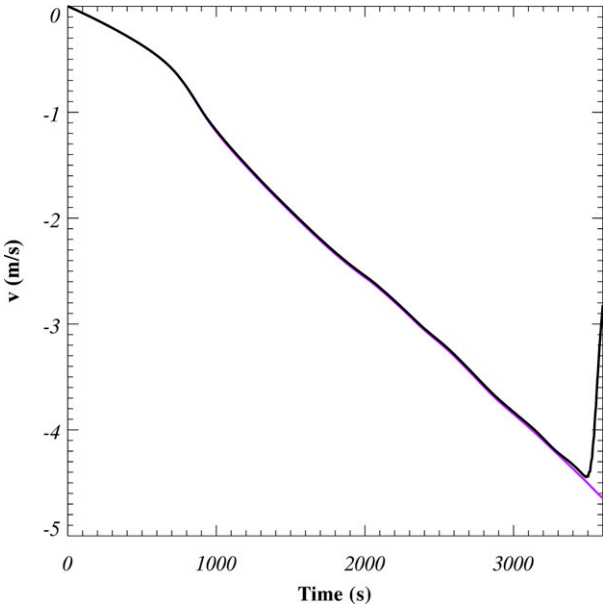

FIG. 4. Simulated (black) and theoretical (purple) v for a near-surface trajectory within the simulated density current of simulations with $d\bar{u}/dz = 0.008\,\mathrm{s}^{-1}$, $d\bar{v}/dz = 0\,\mathrm{s}^{-1}$, $\Delta\theta = -6$ K, and $J_0 = 0.06$ K s^{-1}.

- isolate the indirect impact of boundary-normal shear on ζ_{ns}, separate from its potential direct impact on ζ_{ns},
- characterize the means by which barotropic horizontal vorticity associated with the boundary-parallel shear can impact ζ_{ns},
- isolate the impact of temperature perturbation within the parent air mass of the boundary on ζ_{ns} and consider how this might alter the impact from vertical shear, and

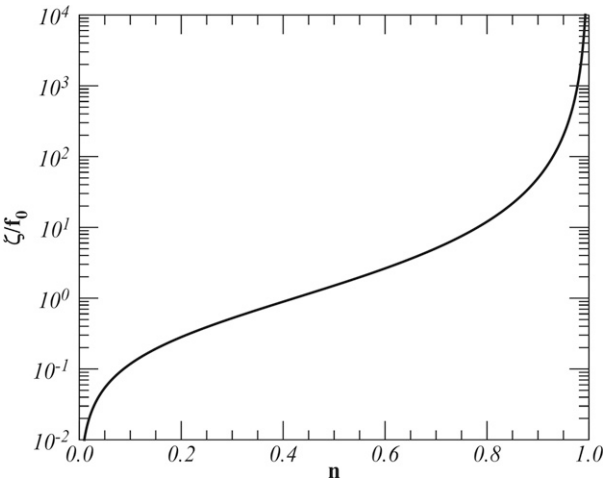

FIG. 5. Theoretical ratio of ζ to f_0 as a function of the amount of fractional contraction of a circuit (n) based on (5).

- characterize how positive buoyancy within surmounting deep convection might alter the impact from vertical shear.

This article proceeds with a description of the experiment design. Results will be presented in section 3 with conclusions and discussion of the results in section 4.

2. Experiment design

The ICOMMAS model (Houston and Wilhelmson 2012) is used for the simulations conducted for this work. The dynamic equations and methods used to solve them are the same in this version of ICOMMAS as in the version used in prior work (e.g., Houston and Niyogi 2007; Houston and

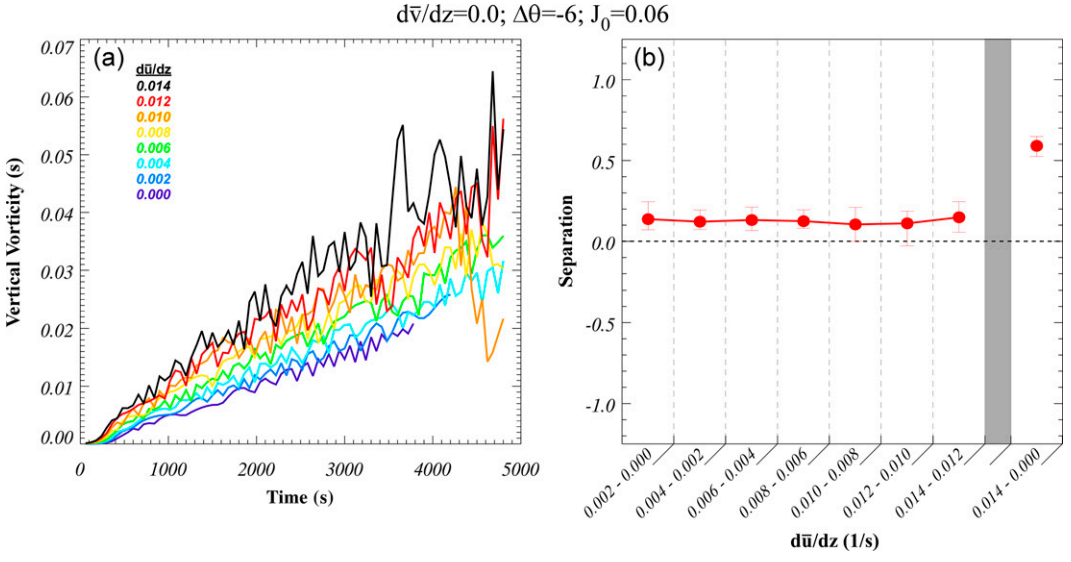

FIG. 6. Maximum ζ_{ns} for the $\partial\bar{u}/\partial z$ experiment set for $d\bar{v}/dz = 0\,\mathrm{s}^{-1}$, $\Delta\theta = -6$ K, and $J_0 = 0.06$ K s^{-1}. (a) Time series and (b) median separations [calculated using (3)] across all times along with the interquartile range illustrated with "whiskers." Filled circles in (b) represent separations that are statistically significant at the 99% level. Separation between experiments with the largest and smallest $\partial\bar{u}/\partial z$ are plotted in the rightmost column in (b).

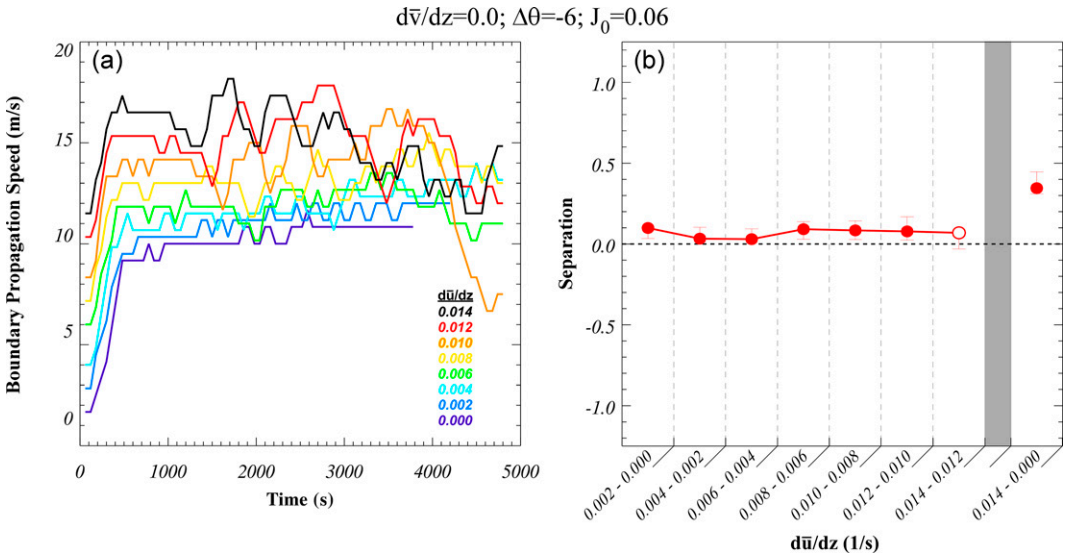

FIG. 7. As in Fig. 6, but for boundary propagation speed.

Wilhelmson 2011, 2012; Laflin and Houston 2012; Houston 2016) except that the Thuburn 3D universal flux limiter (Thuburn 1995) is applied to the wind components as well as scalars. The 2D computational domain is 50 km long (x direction) and 15 km tall. The horizontal grid point spacing is 100 m and the vertical grid point spacing is 50 m in the lowest 1 km but geometrically stretches to 200 m at the top of the domain. Boundary conditions are open/radiative in the x direction. Lower and upper boundary conditions are rigid and free slip. Surface fluxes of heat and moisture, topography, and surface drag are all excluded. Subgrid turbulence is parameterized using the 1.5-order closure parameterization of Klemp and Wilhelmson (1978). Coriolis acceleration is applied to all three components of motion and acts on perturbation wind only (the base state is presumed to be geostrophically balanced). An f plane is assumed with $f_0 = 1.02 \times 10^{-4}\ \mathrm{s}^{-1}$.

Airmass boundaries are initialized using a dam break (e.g., Droegemeier and Wilhelmson 1987; Chen 1995; Liu and Moncrieff 1996; Lee and Wilhelmson 1997; Houston and Wilhelmson 2011, 2012; Houston 2016). The initial cold block is surface based, hydrostatically balanced, and has a minimum potential temperature perturbation that is denoted $\Delta\theta$ (the range of $\Delta\theta$ used for these experiments is listed in Table 1). The potential temperature perturbation within the block is defined as

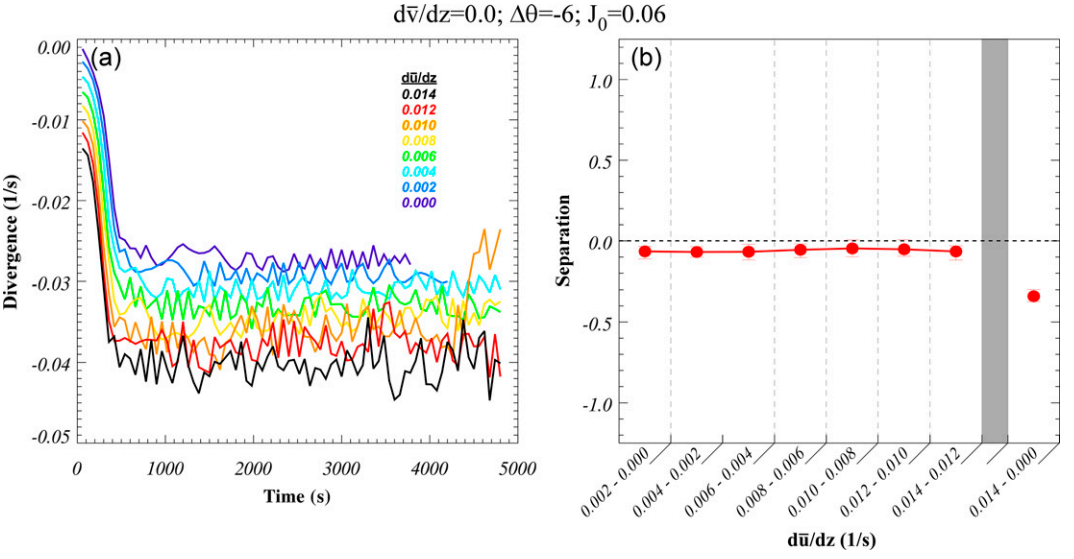

FIG. 8. As in Fig. 6, but for minimum near-surface divergence within 2500 m either side of the airmass boundary.

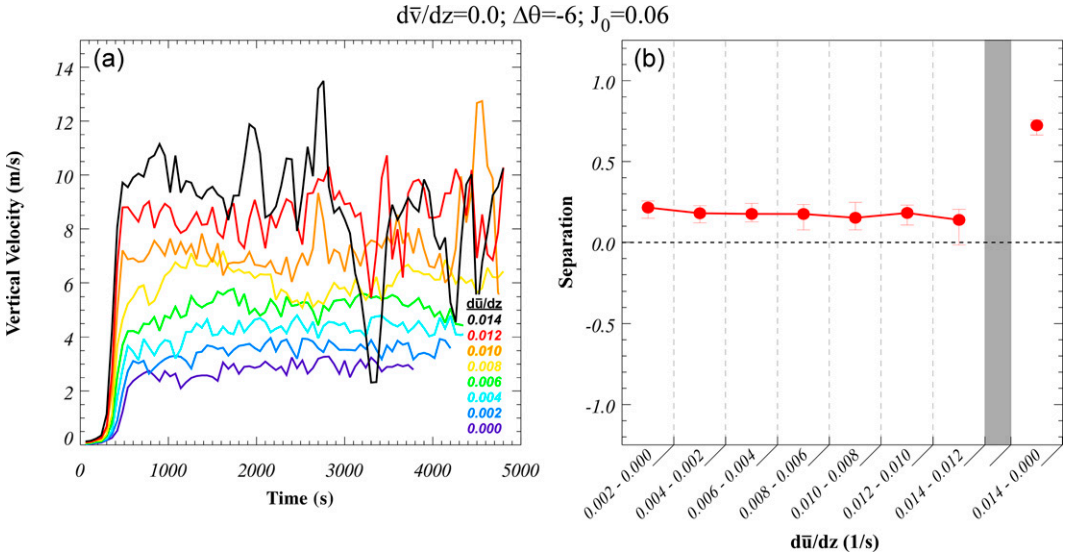

FIG. 9. As in Fig. 6, but for maximum vertical velocity within cold air and within 2500 m of the airmass boundary.

$$\theta' = \frac{1}{2}\Delta\theta[\cos(\pi R) + 1],$$

for $R < 1$, where $R = (r_x^2 + r_z^2)^{1/2}$, $r_x = (x - x_c)/\delta x$ for $x > x_c$ and $r_x = 0$ for $x < x_c$, $r_z = z/\delta z$, $x_c = 5000$ m, $\delta x = 5000$ m, and $\delta z = 2000$ m. The resulting block has a depth (δz) of 2000 m, occupies the western $x_c + \delta x = 10000$ m of the domain, and has a rounded "nose" east of $x < x_c$. Perturbation potential temperature within the portion of the cold block west of x_c is held fixed throughout the simulation, which imposes a constant positive hydrostatic pressure perturbation. As in prior work (e.g., Houston 2016), the u component of the wind within the block is set to be calm when the block is imposed but is not held fixed. The v component of the wind is not altered.

All simulations are dry, thus deep convection is realized through parameterized diabatic heating following a technique similar to that of Houston (2016). However, in contrast to prior work using parameterized diabatic heating (e.g., Markowski and Richardson 2014; Houston 2016), heating is only turned on when air is forced to rise, ostensibly by the airmass boundaries. Specifically, diabatic heating is turned on in ascending air ($w \geq w_0$ where $w_0 = 0.1$ m s^{-1} for this work) at grid points above a fixed height (denoted z_{LCL}, set to 1000 m for this work) provided that the air at these points originated below z_{LCL} and is only weakly diluted. The condition on air source and dilution is imposed using a tracer (q) that is initialized with a concentration of 12 g kg^{-1} below z_{LCL}. If $q \geq q_0$ (where $q_0 = 10$ g kg^{-1} for this work) then the source and dilution conditions are met. The conditions are summarized with the following expression:

$$J(x,z) = \begin{cases} \hat{J}(z); & w \geq w_0 \text{ and } q \geq q_0 \\ 0; & w < w_0 \text{ or } q < q_0 \end{cases},$$

where

$$\hat{J}(z) = J_0 \frac{z}{z_m}\left[\frac{1 - \beta z/z_m}{1 - \beta}\right]^{(\beta^{-1}-1)},$$

where J_0 is the maximum $\hat{J}$ and serves as a free parameter (Table 1), z_m is the height of maximum $\hat{J}$, and β is a

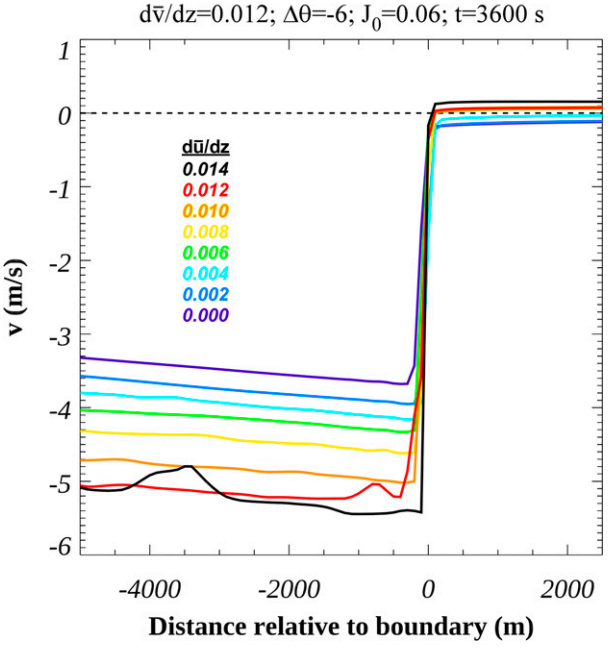

FIG. 10. Lateral distribution of v relative to boundary position at 3600 s for the $\partial\bar{u}/\partial z$ experiment set for $d\bar{v}/dz = 0\,\text{s}^{-1}$, $\Delta\theta = -6$ K, and $J_0 = 0.06$ K s^{-1}.

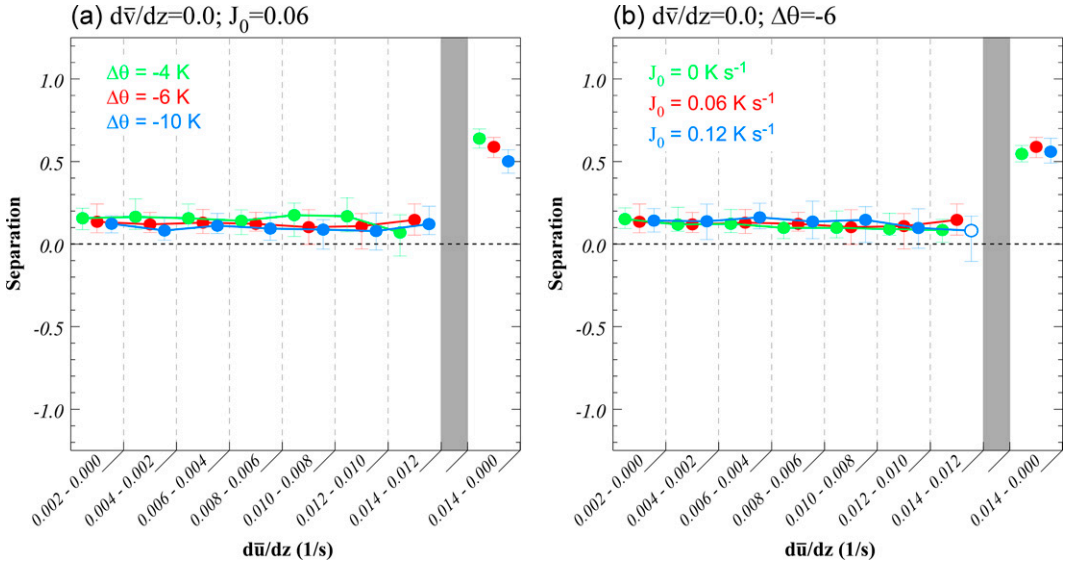

FIG. 11. As in Fig. 6b, but for (a) $\Delta\theta$ of -4 K (green), -6 K (red), and -10 K (blue) and (b) J_0 of 0 K s^{-1} (green), 0.06 K s^{-1} (red), and 12 K s^{-1} (blue).

coefficient that, together with z_m, dictates the total height of diabatic heating ($z_1 = z_m/\beta$). This formulation differs somewhat from the expression used by Houston (2016) and was selected so that the height of maximum $\hat{J}$ could be lowered in a reasonable way. Only J_0 is treated as a free parameter for this work; other tunable parameters are held fixed: $z_m = 3333$ m and $\beta = 1/3$ and thus $z_1 = 10000$ m. The vertical profile of $\hat{J}$ for $J_0 = 0.06$ K s^{-1} appears in Fig. 1. Through this technique, diabatic heating and resultant deep tropospheric ascent are tunable. Moreover, because of the exclusion of moisture (precipitation), density current temperature perturbation remains a free parameter.

The base state temperature profile is prescribed such that $d\bar{\theta}/dz$ is 0.001 K m^{-1} below z_1 and 0.025 K m^{-1} above z_1. The base state vertical profile of wind is prescribed such that the boundary-normal vertical shear ($d\bar{u}/dz$) and boundary-parallel vertical shear ($d\bar{v}/dz$) are constant below a height of 1000 m, and are specified as free parameters whose

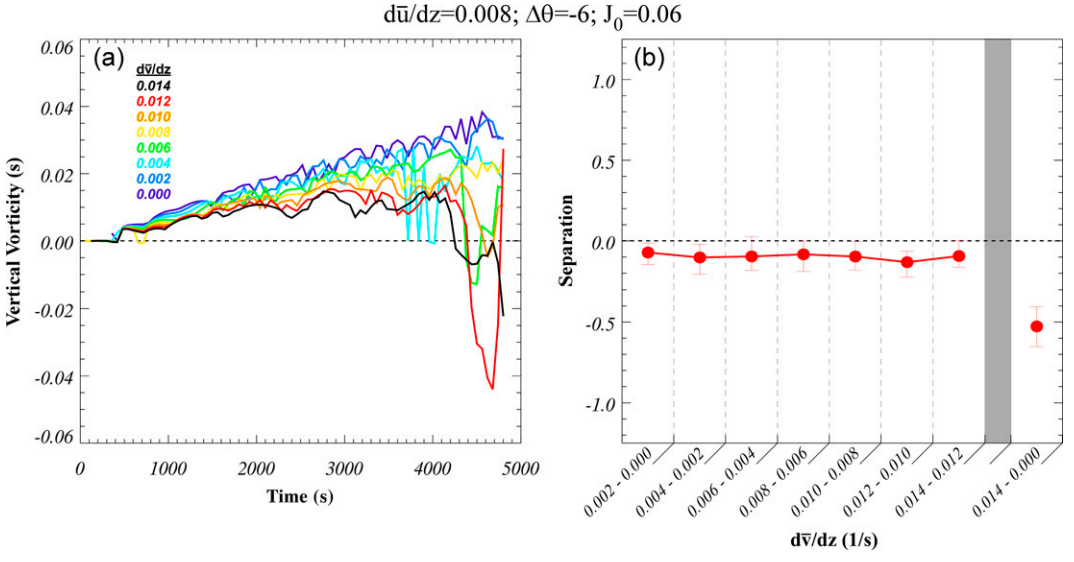

FIG. 12. Maximum ζ_{ns} for the $\partial\bar{v}/\partial z$ experiment set for $d\bar{u}/dz = 0.008\,\text{s}^{-1}$, $\Delta\theta = -6$ K, and $J_0 = 0.06$ K s^{-1}. (a) Time series and (b) median separations [calculated using (3)] across all times along with the interquartile range illustrated with "whiskers." Filled circles in (b) represent separations that are statistically significant. Separation between experiments with the largest and smallest $\partial\bar{v}/\partial z$ are plotted in the rightmost column in (b).

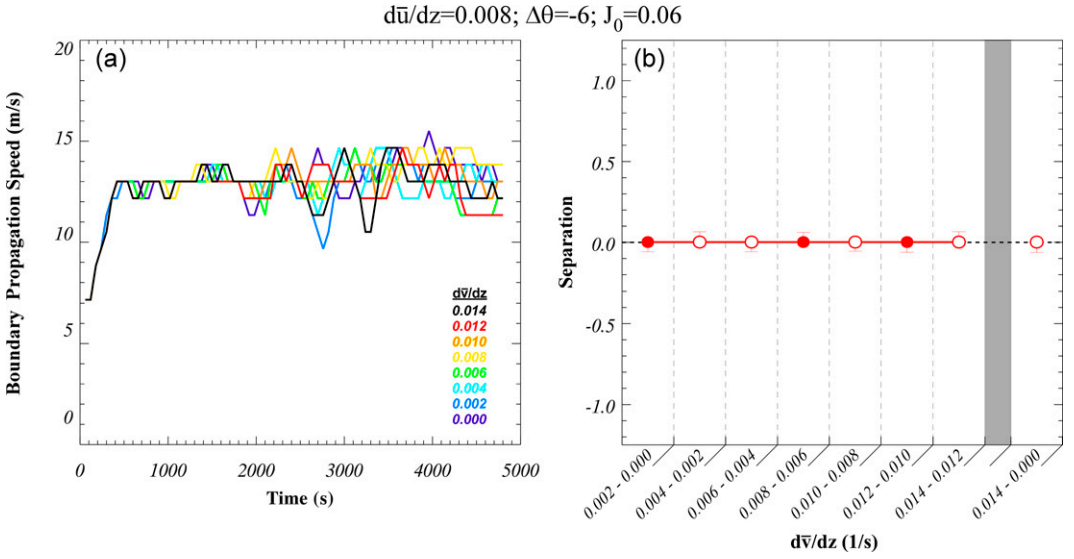

FIG. 13. As in Fig. 12, but for boundary propagation speed.

values are listed in Table 1. The wind at 1000 m is calm and, thus, for nonzero vertical shear, the strongest flow is at the surface (Fig. 2).

Analysis will focus on the sensitivity of near-surface ζ (at the lowest model grid level, $z = 25$ m, denoted ζ_{ns}) which, for 2D (x–z) slab symmetry, is equivalent to $\partial v/\partial x$. For x–z slab symmetry, the Lagrangian rate of change (D/Dt) of ζ:

$$\frac{D\zeta}{Dt} = -\delta\zeta - \delta f_0 - \frac{\partial w}{\partial x}\frac{\partial v}{\partial z}, \tag{1}$$

where δ is divergence, illustrates the three sources of ζ: stretching of relative vorticity, stretching of planetary vorticity, and tilting of the x component of barotropic horizontal vorticity ($\omega_x = -\partial v/\partial z$). The ω_x will exist at initialization provided $\partial\overline{v}/\partial z \neq 0$ and, based on

$$\frac{D}{Dt}(\omega_x) = -\omega_x\frac{\partial w}{\partial z} - \frac{\partial u}{\partial z}\frac{\partial v}{\partial x} - f_0\frac{\partial u'}{\partial z}, \tag{2}$$

can be generated through stretching [first term on the right-hand side of (2)], tilting, and the action of the Coriolis force on $\partial u'/\partial z$, where u' is perturbation zonal wind. (As noted previously, the solenoidal generation of ω_x is absent for x–z slab symmetry.)

Focus of this analysis is directed toward the maximum/minimum ζ_{ns} defined as the first/easternmost critical point behind (west of) the airmass boundary (defined based on $\theta' < -0.1$ K). This maximum/minimum is not a global maximum/minimum at the lowest model grid level nor is it a maximum/minimum within some threshold distance from the airmass boundary.

To quantify the separation between time series of a particular sensitivity variable (e.g., ζ_{ns}) across a set of parameter values (e.g., $d\overline{u}/dz = 0.008$), a quantity defined as "separation" (Δ) will be used:

$$\Delta = \frac{\phi_j(t) - \phi_k(t)}{\max[|\phi_j(t)| - |\phi_k(t)|]}, \tag{3}$$

where $\phi_j(t)$ is the value of the sensitivity variable for value j of a parameter variable at time t and $\phi_k(t)$ is the value of the sensitivity variable for a different value (k) of the parameter variable. The median separation (across all times), along with the interquartile range, will be reported. To assess the significance of separation at the 99th percentile we use the two-tailed Wilcoxon signed-rank method, which quantifies the likelihood that the median separation is zero. This nonparametric test is appropriate since, based on a Kolmogorov–Smirnov normalization test, none of the separation distributions reported here are normal. Unless otherwise noted, analysis considers simulation results from $t = 60$ s to $t = 4800$ s or the time when the density current reaches a position within 10 km of the eastern domain boundary, whichever comes first.[1]

3. Results

a. Sensitivity to boundary-normal shear ($d\overline{u}/dz$)

In agreement with prior studies (e.g., Rotunno et al. 1988; Xu 1992; Xue et al. 1997; Bryan and Rotunno 2014), the depth

[1] Of the 81 simulations whose results are used in this work, 23 were truncated because the density current was within 10 km of the eastern boundary. Of these 23, 3 were truncated between 4200 and 4800 s, 11 between 3600 and 4200s, 7 between 3000 and 3600 s, and 2 between 2400 and 3600 s.

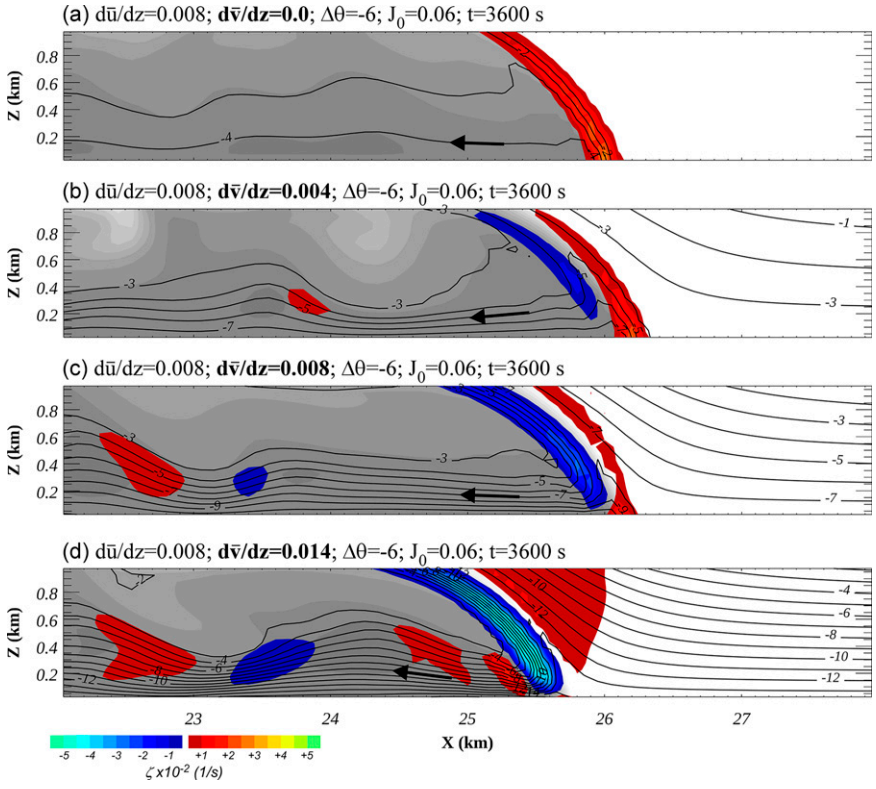

FIG. 14. The ζ_{ns} (shaded in color), $\theta' < 0$ (shaded in grayscale every 0.5 K), and v (contoured every 1 m s^{-1}) at 3600 s for the simulations in which $d\bar{u}/dz = 0.008\,\mathrm{s}^{-1}$, $\Delta\theta = -6$ K, $J_0 = 0.06$ K s^{-1}, and (a) $d\bar{v}/dz = 0\,\mathrm{s}^{-1}$, (b) $d\bar{v}/dz = 0.004\,\mathrm{s}^{-1}$, (c) $d\bar{v}/dz = 0.008\,\mathrm{s}^{-1}$, and (d) $d\bar{v}/dz = 0.014\,\mathrm{s}^{-1}$. Arrows denote the direction of vorticity at select points.

of the density current head and the uprightness of the vertical jet along the current's sloped leading edge scale directly with $d\bar{u}/dz$ (Fig. 3).[2] With the Coriolis force turned on, ζ is positive along the boundary and maximized near the surface and on the cold side of the airmass boundary (Fig. 3). *Without Coriolis, no ζ is generated.* Values of ζ_{ns} by 3600 s (for $d\bar{u}/dz = 0.008\,\mathrm{s}^{-1}$) approach 0.03 s^{-1} (Fig. 3); thus, even in the absence of baroclinically generated ζ, ζ_{ns} values more than two orders of magnitude larger than planetary vorticity are possible after only one hour.

A trajectory released within the initial cold block, integrated forward through the entire simulation,[3] and passing through the region of large ζ behind the airmass boundary reveals the generation of a meridional component of the flow (black curve in Fig. 4) that is consistent with the theoretical generation (purple curve in Fig. 4) calculated using the simulated perturbation zonal flow (i.e., $v = -f_0 \int u'\,dt$). Thus, the generated meridional flow and associated ζ are consistent with theory. The difference between the simulated and theoretical v apparent between 3500 and 3600 s is likely attributable to significant mixing near the boundary that contributes to a momentum sink in this region.

To further expand on the theoretical contribution of planetary vorticity to the generation of ζ over the time scales relevant for this work, we consider the circulation equation:

$$\frac{DC}{Dt} = -f_0 \frac{DA}{Dt}, \tag{4}$$

where C is the relative circulation, f_0 is the planetary vorticity, and A is the area of a rectangular circuit whose width compresses in time as if in the presence of convergence near a boundary. Assuming an f plane, this scenario yields

$$\frac{\zeta}{f_0} = \frac{n}{1-n}, \tag{5}$$

where n is the fractional reduction of the rectangular circuit's width. According to (5), and illustrated in Fig. 5, a contraction of 50% (regardless of the rate of contraction) is sufficient to

[2] The full parameter space considered by Rotunno et al. (1988) included conditions in which vertical shear was so strong relative to the cold pool circulation that the uprightness of the vertical jet decreased with increasing shear. However, the environments considered here do not include such conditions.

[3] Trajectories are integrated forward using fourth-order Runge–Kutta at a data time interval of 1 s (no temporal interpolation is performed). State values are bilinearly interpolated to trajectory positions.

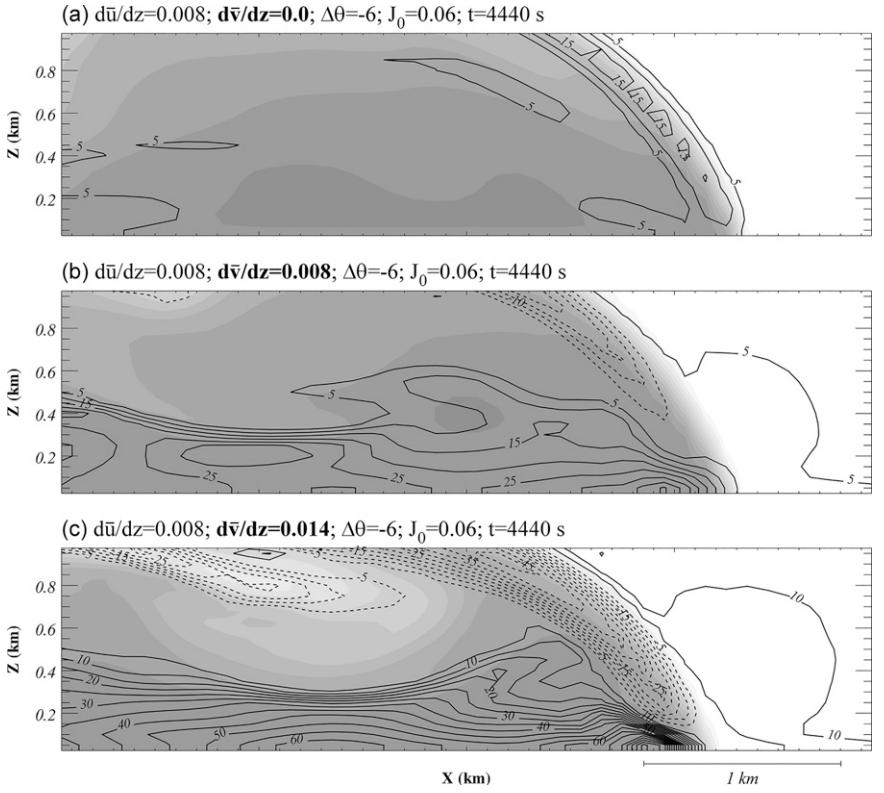

FIG. 15. The $\partial v/\partial z$ (contoured every 5×10^{-3} s^{-1}) and $\theta' < 0$ (shaded in grayscale every 0.5 K) at 4440 s for the simulations in which $d\bar{u}/dz = 0.008\,\mathrm{s}^{-1}$, $\Delta\theta = -6$ K, $J_0 = 0.06$ K s^{-1}, and (a) $d\bar{v}/dz = 0\,\mathrm{s}^{-1}$, (b) $d\bar{v}/dz = 0.008\,\mathrm{s}^{-1}$, and (c) $d\bar{v}/dz = 0.014\mathrm{s}^{-1}$.

increase ζ to a value of f_0 and $n \sim 91\%$ for ζ to become an order of magnitude larger than f_0. For the simulations conducted for this work, the simulated $\zeta_{ns} \approx 0.03$ s^{-1} is consistent with a contraction of 99.1%.

The magnitude of ζ_{ns} is found to increase with increasing $d\bar{u}/dz$ (Fig. 6a) with statistically significant intraexperiment separations (Fig. 6b). The relationship between $d\bar{u}/dz$ and boundary propagation speed (with the surface wind subtracted, Fig. 7), minimum near-surface divergence ($\partial u/\partial x$) within 2500 m of the airmass boundary (Fig. 8), and maximum vertical velocity within the cold air of the density current head (defined as air with a perturbation potential temperature $\leq 50\%$ of $\Delta\theta$ and located within 2500 m of the airmass boundary; Fig. 9) generally mimic the pattern exhibited between $d\bar{u}/dz$ and ζ. This similarity is consistent with theory (Houston 2016). Moreover, this relationship supports the hypothesis that, in 2D, ζ_{ns} sensitivity to boundary-normal shear is a consequence of faster boundary propagation speed.

The above result is consistent with the generation of circulation and ζ through circuit contraction in a rotating frame of reference (4). A different perspective on the increase in ζ with faster propagation speed is afforded through analysis of the distributions of v across the eight $d\bar{u}/dz$ experiments (Fig. 10) which show that v is more negative for larger $d\bar{u}/dz$. This pattern is a consequence of the action of the Coriolis force on larger perturbation zonal wind (u') for larger $d\bar{u}/dz$. Recall that $d\bar{u}/dz$ in these experiments is imposed along with more negative u (Fig. 2). If boundary propagation speed was constant across all $d\bar{u}/dz$ simulations, then u' within the density current would be largely insensitive to $d\bar{u}/dz$ and so would v. However, because boundary propagation speed scales directly with $d\bar{u}/dz$, the magnitude of u' and v do as well.

When $\Delta\theta$ is increased to -4 K or decreased to -10 K the overall sensitivity of ζ_{ns} to $d\bar{u}/dz$ does not change: ζ_{ns} is still directly related to $d\bar{u}/dz$ (Fig. 11a). This result does show that the sensitivity of vortex sheets to $d\bar{u}/dz$ is somewhat less significant for colder, faster-moving density currents. This result does not reflect the overall sensitivity of ζ_{ns} to $\Delta\theta$, a sensitivity that will be discussed in section 3d. When J_0 is increased to 0.12 K s^{-1} or decreased to 0, the overall sensitivity of ζ_{ns} to $d\bar{u}/dz$ does not change (Fig. 11b).

Referring back to the mechanisms by which vertical shear could impact ζ_{ns} summarized in section 1, it can be concluded that $d\bar{u}/dz$ impacts ζ_{ns} through "Indirect 2": vertical shear alters boundary propagation speed. The "Direct" mechanism is not relevant because of slab symmetry and horizontal vorticity parallel to the boundary. "Indirect 3" is not the dominant process regulating vortex sheet magnitude because maximum ζ_{ns} is found on the cold side of the airmass boundary. Separations in ζ_{ns} as a

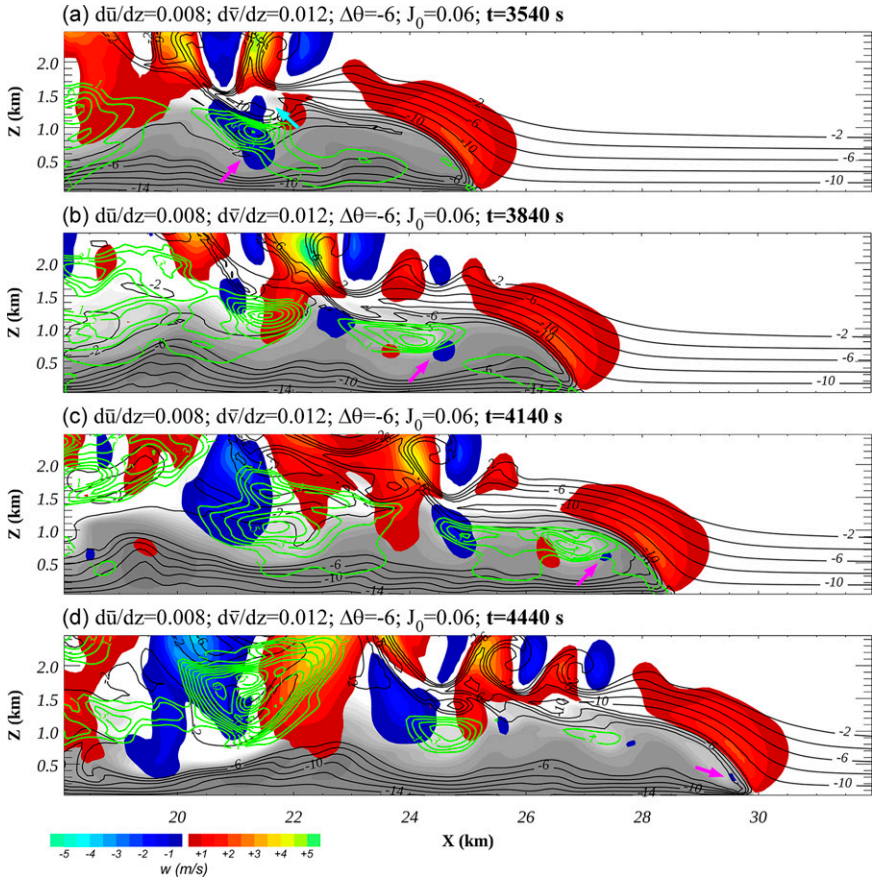

FIG. 16. Vertical velocity (shaded in color), $\theta' < 0$ (shaded in grayscale every 0.5 K), v (contoured in black every 1 m s^{-1}), and boundary-relative $u > 0$ (contoured in green every 1 m s^{-1}) for the $d\bar{u}/dz = 0.008\,\mathrm{s}^{-1}$, $d\bar{v}/dz = 0.012\,\mathrm{s}^{-1}$, $\Delta\theta = -6$ K, $J_0 = 0.06$ K s^{-1} simulation at (a) 3540, (b) 3840, (c) 4140, and (d) 4440 s. Pink arrows point to a penetrative downdraft and the blue arrow in (a) points to a KH gyre.

function of $d\bar{u}/dz$ show no coherent sensitivity to J_0; thus, phasing of ζ_{ns} with above-surface VPGF associated with positive buoyancy ("Indirect 4") is likely of minimal importance.

b. *Sensitivity to boundary-parallel shear ($d\bar{v}/dz$)*

In all experiments designed to test the sensitivity of ζ_{ns} to $d\bar{v}/dz$, $\zeta_{ns} > 0$ is generated immediately on the dense side of the airmass boundary (Fig. 12).[4] However, unlike in the $d\bar{u}/dz$ experiments for which ζ_{ns} scales directly with the magnitude of the shear, ζ_{ns} is found to scale inversely with $d\bar{v}/dz$ (Fig. 12) with separations that are statistically significant (Fig. 12b). Moreover, although initially positive, in the experiments with the largest $d\bar{v}/dz$, ζ_{ns} becomes negative immediately behind the airmass boundary (Fig. 12a).

In contrast to the $d\bar{u}/dz$ experiments, the sensitivity of ζ_{ns} to $d\bar{v}/dz$ is not a consequence of differences in boundary propagation speed (Fig. 13). Instead, the reduction in positive ζ_{ns} is due to the increasing (with $d\bar{v}/dz$) impact of upward tilting of negative zonal horizontal vorticity within the density current. (Recall that the cold block is initialized with the same $d\bar{v}/dz$ as the environment ahead of the block.) This is clearly illustrated via isotachs of the v component of the wind (Fig. 14), which serve as proxies for vortex lines in 2D with slab symmetry in the y direction (the direction of vorticity is indicated by arrows in Fig. 14). Note that as $d\bar{v}/dz$ increases, the region of negative ζ "lowers" toward the region of ζ_{ns} at the airmass boundary.

The contribution to ζ from tilting of $\partial v/\partial z$ is seen in the vorticity equation for a slab-symmetric frame of reference (1) from which it is clear that, on the backside of the airmass boundary, where $\partial w/\partial x > 0$, $\zeta < 0$ will be generated. In fact, because the slab-symmetric version of the tendency equation for $\partial v/\partial z$ includes the action of the Coriolis force on $\partial u'/\partial z$ (2), tilting will contribute to negative ζ even when $d\bar{v}/dz = 0$ since zonal shear is generated within the density current (not shown). However, by a little over one hour into the

[4] Recall that ζ_{ns} is defined as the first critical point behind the boundary. As such, if positive ζ_{ns} is found immediately behind the boundary but larger magnitude negative values are found farther into the cold air, the maximum value is reported as positive since this would correspond to the first critical point behind the boundary.

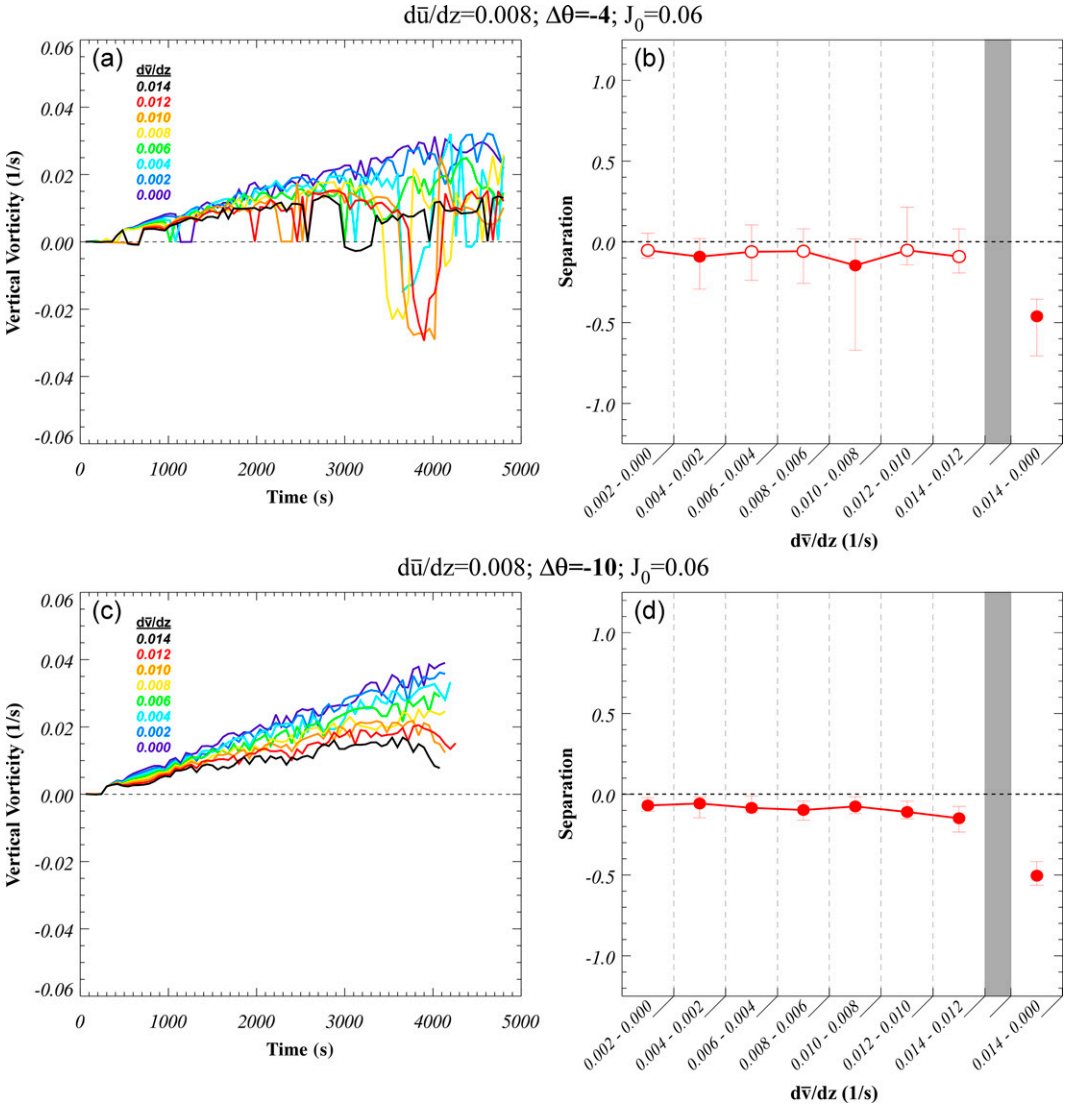

FIG. 17. As in Fig. 12, but for (a),(b) $\Delta\theta = -4$ K and (c),(d) $\Delta\theta = -10$ K.

simulations, the magnitude of the resulting $\partial v/\partial z$ is ~5 times (~15 times) larger for $d\bar{v}/dz = 0.008\,\mathrm{s}^{-1}$ ($d\bar{v}/dz = 0.014\,\mathrm{s}^{-1}$) compared to $d\bar{v}/dz = 0$ (Fig. 15).

Despite the contribution to negative ζ from tilting of $\partial v/\partial z$, the leading ζ_{ns} is positive for the majority of the integration in all simulations within the $d\bar{v}/dz$ experiment set (Fig. 12). To some degree this can be attributed to the fact that most of the tilting of $\partial v/\partial z$ occurs in rising air; thus, negative ζ manifests principally above the lowest model grid level. Nevertheless, the transition to negative leading-edge ζ_{ns} does occur in several of the simulations (Fig. 12). This transition is associated with a forward-propagating (boundary-relative) penetrative downdraft within the density current (pink arrows in Fig. 16). The penetrative downdraft is a consequence of the coupling of a KH gyre (light blue arrow in Fig. 16a) and dynamic downdraft associated with free convection above the density current. The induced positive boundary-relative flow advects the downdraft toward the boundary where it drives vortex lines toward the surface (Fig. 16c), amplifying negative ζ_{ns}. The likelihood of this transition is generally higher for larger $d\bar{v}/dz$ but a consistent relationship between the magnitude of negative ζ_{ns} and $d\bar{v}/dz$ is not apparent. Instead, the overall impact of downdraft-driven generation of negative ζ_{ns} is to increase the temporal variability in ζ_{ns}.

Increasing $\Delta\theta$ from -6 to -4 K reduces the number of $d\bar{v}/dz$ simulations whose ζ_{ns} separations are significant (cf. Fig. 12 and Figs. 17a,b). This appears to be a consequence of more interexperiment variability in the sign of ζ_{ns} in the -4 K simulations compared to the -6 K simulations. The trend of decreasing variability with colder $\Delta\theta$ is also reflected in simulations conducted with $\Delta\theta = -10$ K (Figs. 17c,d). Also of note in the -10 K simulations is that ζ_{ns} is never less than

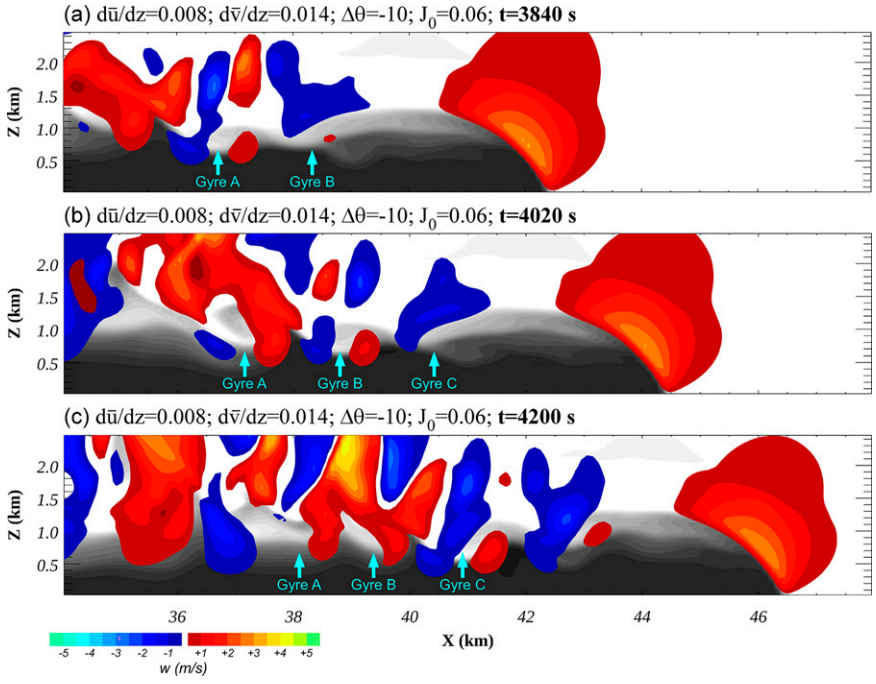

FIG. 18. Vertical velocity (shaded in color) and $\theta' < 0$ (shaded in grayscale every 0.5 K) for the $d\bar{u}/dz = 0.008\,\mathrm{s}^{-1}$, $d\bar{v}/dz = 0.014\,\mathrm{s}^{-1}$, $\Delta\theta = -10$ K, $J_0 = 0.06$ K s^{-1} simulation at (a) 3840, (b) 4020, and (c) 4200 s.

zero (Fig. 17c). Both the reduction in variability and absence of $\zeta_{ns} < 0$ in the −10 K simulations are attributable to the inability of wake gyres to propagate toward the airmass boundary given its faster motion relative to warmer cold blocks (Fig. 18). By extension, the higher variability and more rapid transition to negative ζ_{ns} in the −4 K simulations can be attributed to the forward (relative to the airmass boundary) propagation of wake gyres (not shown).

The sensitivity of ζ_{ns} to $d\bar{v}/dz$ depends on J_0 in a manner similar to how the sensitivity of ζ_{ns} to $d\bar{v}/dz$ depends on $\Delta\theta$. Namely, with increasing J_0, the number of $d\bar{v}/dz$ simulations whose ζ_{ns} separations are significant decreases because there is more variability in the sign of ζ_{ns} for larger values of J_0 (Fig. 19). Moreover, as with $\Delta\theta$, variability is controlled by the ability of wake gyres to propagate forward. Analogous to colder cold blocks, smaller J_0 supports faster boundary propagation speed (Fig. 20). (The sensitivity of boundary propagation speed and ζ_{ns} exclusively to J_0 will be examined in future work). Faster boundary propagation speed in the small J_0 simulations prevents the forward propagation of gyres, which can amplify negative ζ_{ns} at the boundary and yield the variability that is seen in the higher J_0 simulations (Fig. 19b).

These results indicate that the sensitivity of ζ_{ns} to $d\bar{v}/dz$ is explained through the "Direct" mechanism described in section 1: horizontal vorticity associated with the vertical shear contributes directly to the vortex sheet. The sensitivity is not a consequence of changes in boundary propagation speed ("Indirect 2" or "Indirect 3"). Furthermore, it unlikely to be a consequence of changes in phasing with above-surface VPGF ("Indirect 4") since a systematic increase in ζ_{ns} is not simulated when J_0 is increased.

c. *Sensitivity to cold block temperature ($\Delta\theta$)*

An inverse and statistically significant relationship exists between ζ_{ns} and $\Delta\theta$ (Figs. 21a,b). This relationship is a direct consequence of the dependence of boundary propagation speed and divergence on $\Delta\theta$ (Fig. 22) and exists despite the increased stability of the colder density currents. Consistent with RKW theory (Rotunno et al. 1988), the updraft at the density current leading edge is more erect for warmer density currents (Fig. 23). However, even with the improved "phasing" of the updraft relative to the vorticity at the airmass boundary for the warmer density currents (Houston 2016), ζ_{ns} is still larger for colder density currents.

4. Conclusions and discussion

Research presented here aimed to identify the theoretical impact of the following three characteristics on the strength of vortex sheets along airmass boundaries: 1) boundary-normal component of the vertical wind shear, 2) boundary-parallel component of the vertical wind shear, and 3) temperature perturbation within the parent air mass of the boundary. Numerical experiments of density currents were conducted in a 2D domain with parameterized latent heating for convection initiated at the associated airmass boundary and

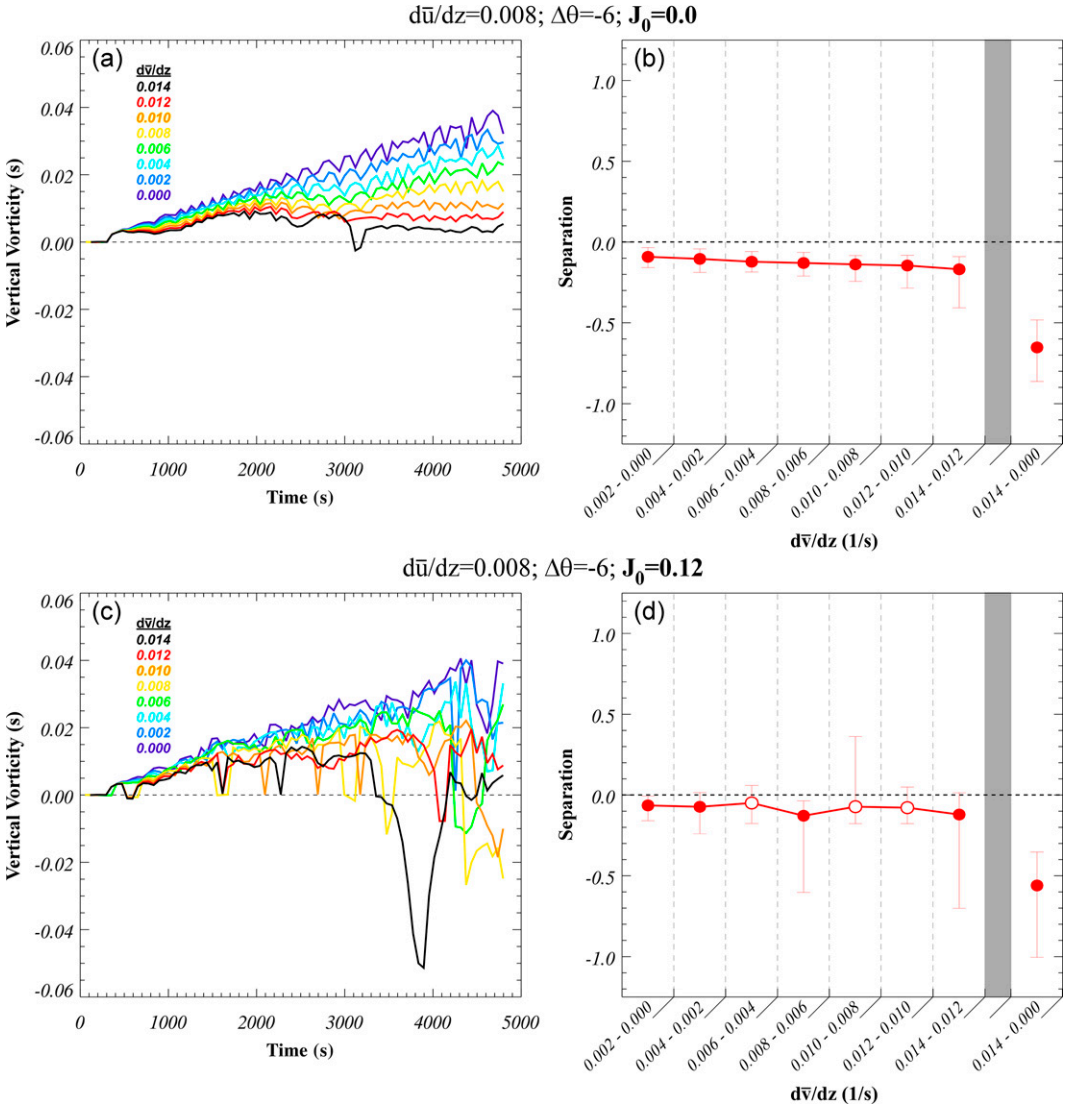

FIG. 19. As in Fig. 12, but for (a),(b) $J_0 = 0$ K s^{-1} and (c),(d) $J_0 = 0.12$ K s^{-1}.

Coriolis turned on. Principal conclusions from analysis of these experiments are as follows:

- With Coriolis turned on and without any boundary-parallel shear ($d\bar{v}/dz$) ζ_{ns} is positive along the boundary and located on the cold side of the boundary. Without Coriolis no ζ is generated without $d\bar{v}/dz$. Vortex sheets with $\zeta_{ns} > 0.05$ s^{-1} after approximately one hour can be simulated without baroclinicity or above-surface VPGF tied to ζ.
- The magnitude of ζ_{ns} is found to increase with increasing boundary-normal shear ($d\bar{u}/dz$), all else equal, with statistically significant intraexperiment separations. This sensitivity is attributable to the associated increase in boundary propagation speed (mechanism "Indirect 2" described in section 1).
- The ζ_{ns} is found to scale inversely with $d\bar{v}/dz$. The reduction in positive ζ_{ns} is due to the increasing (with $d\bar{v}/dz$) impact of upward tilting of negative zonal horizontal vorticity within the density current which "lowers" negative ζ toward the region of ζ_{ns} at the airmass boundary. Thus, the "Direct" mechanism for ζ_{ns} generation is relevant in the presence of $d\bar{v}/dz$. The transition to negative leading-edge ζ_{ns} does occur in several of the larger $d\bar{v}/dz$ simulations and is associated with a forward-propagating (boundary-relative) penetrative downdraft within the density current. A consistent relationship between the magnitude of negative ζ_{ns} and $d\bar{v}/dz$ is not apparent; thus, the overall impact of downdraft-driven generation of negative ζ_{ns} is to increase the temporal variability in ζ_{ns}. Both colder $\Delta\theta$ and decreasing J_0 increase the number of $d\bar{v}/dz$ simulations whose ζ_{ns} separations are significant because wake gyres are not able to propagate toward the boundary due to its faster motion relative to simulations with warmer $\Delta\theta$ or larger J_0.

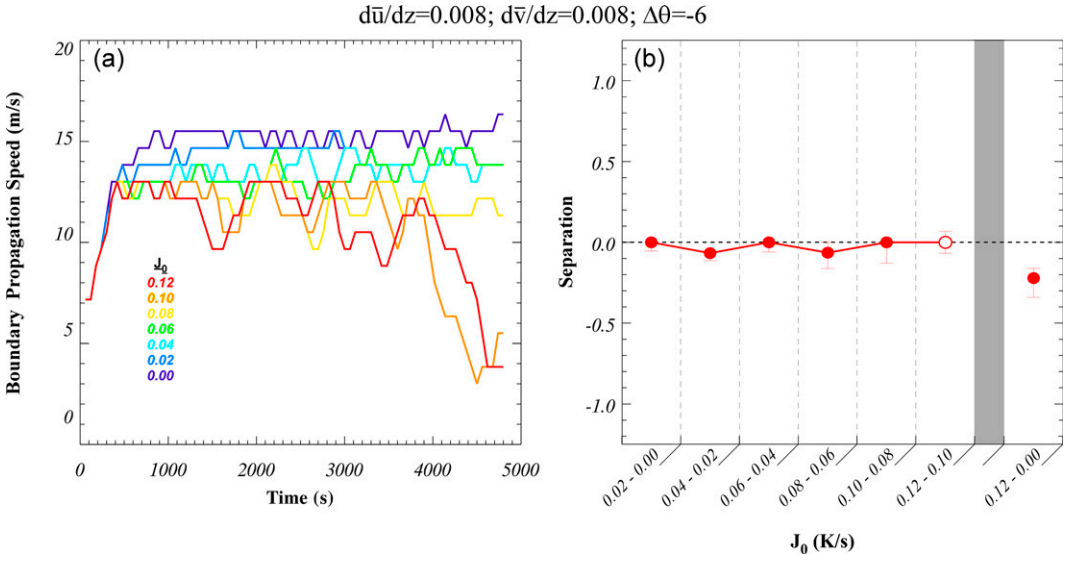

FIG. 20. Boundary propagation speed for the J_0 experiment set for $d\bar{u}/dz = 0.008\,\mathrm{s}^{-1}$, $d\bar{v}/dz = 0.008\,\mathrm{s}^{-1}$, and $\Delta\theta = -6$ K. (a) Time series and (b) median separations [calculated using (3)] across all times along with the interquartile range illustrated with "whiskers." Filled circles in (b) represent separations that are statistically significant. Separation between experiments with the largest and smallest J_0 are plotted in the rightmost column in (b).

- An inverse and statistically significant relationship exists between ζ_{ns} and $\Delta\theta$ and is a direct consequence of the dependence of boundary propagation speed and divergence on $\Delta\theta$. This relationship exists despite the increased stability of the colder density currents and reduced "phasing"/erectness of surmounting buoyant updrafts with the region of positive ζ at the boundary.

Several of the simplifications in the experiment design that have been imposed to isolate processes responsible for vortex sheet amplification could modulate the actual sensitivities to low-level shear and temperature perturbation of the boundary's parent air mass. For example, a 2D framework overdoes turbulent mixing (Bryan and Rotunno 2014). This may result in erroneously large entrainment of ambient air into the boundary's parent air mass. Thus, the penetrative downdrafts which were found in these 2D simulations to generate negative ζ_{ns} at the boundary may be less common in 3D. As such, the generation of $\zeta_{ns} < 0$ due to these penetrative downdrafts when $d\bar{v}/dz > 0$ may be less common (or may not occur at all) in 3D. The overall sensitivity of ζ_{ns} to $d\bar{v}/dz$ captured by these experiments is unlikely to be affected significantly by the 2D framework.

The use of a free-slip lower boundary condition is common in idealized numerical studies but the inclusion of surface friction could change the vertical distribution of vertical vorticity at the airmass boundary. Friction could also alter the boundary propagation and associated convergence. In combination with the inclusion of a third dimension, friction could also provide an additional source for ζ_{ns} (Rotunno et al. 1988; Fovell and Ogura 1989; Schenkman et al. 2012; Markowski 2016), a process that may be sensitive to low-level shear and airmass temperature and thus might modulate the sensitivities documented here.

The exclusion of precipitation is necessary to isolate the sensitivities that serve as the focus of this work but precipitation may create an important feedback that will need to be explored in future work. For example, more erect ascent at an airmass boundary associated with increasing boundary-normal vertical shear would yield a source of cold air, through precipitation evaporation and sublimation, closer to the boundary (Rotunno et al. 1988; Fovell and Ogura 1989). This could alter density current depth and propagation speed and therefore impact ζ_{ns} in a way not captured when precipitation is excluded. It is likely that this feedback would increase the magnitude of the signal found in this work; namely, ζ_{ns} would likely have a more significant relationship to boundary-normal vertical shear.

As noted in the introduction, the overarching objective of this work is to expose the sensitivity of micro-α- to meso-γ-scale vortices along airmass boundaries to environmental conditions. While experiment design simplifications adopted for this work render these results theoretical, some possible implications of these results can be discussed. Given the opposite impacts of boundary-parallel versus boundary-normal shear on vortex sheet intensity, it can be surmised that a favored location for mesovortex development along a curved generally north–south-oriented gust front in an environment with southerly low-level shear would be on the north end of the boundary where the boundary-normal component of vertical shear is largest. Given the dependence of vortex sheet strength on the temperature perturbation of a boundary's parent air mass, it could be hypothesized that higher LCLs will be more favorable for mesovortex development along

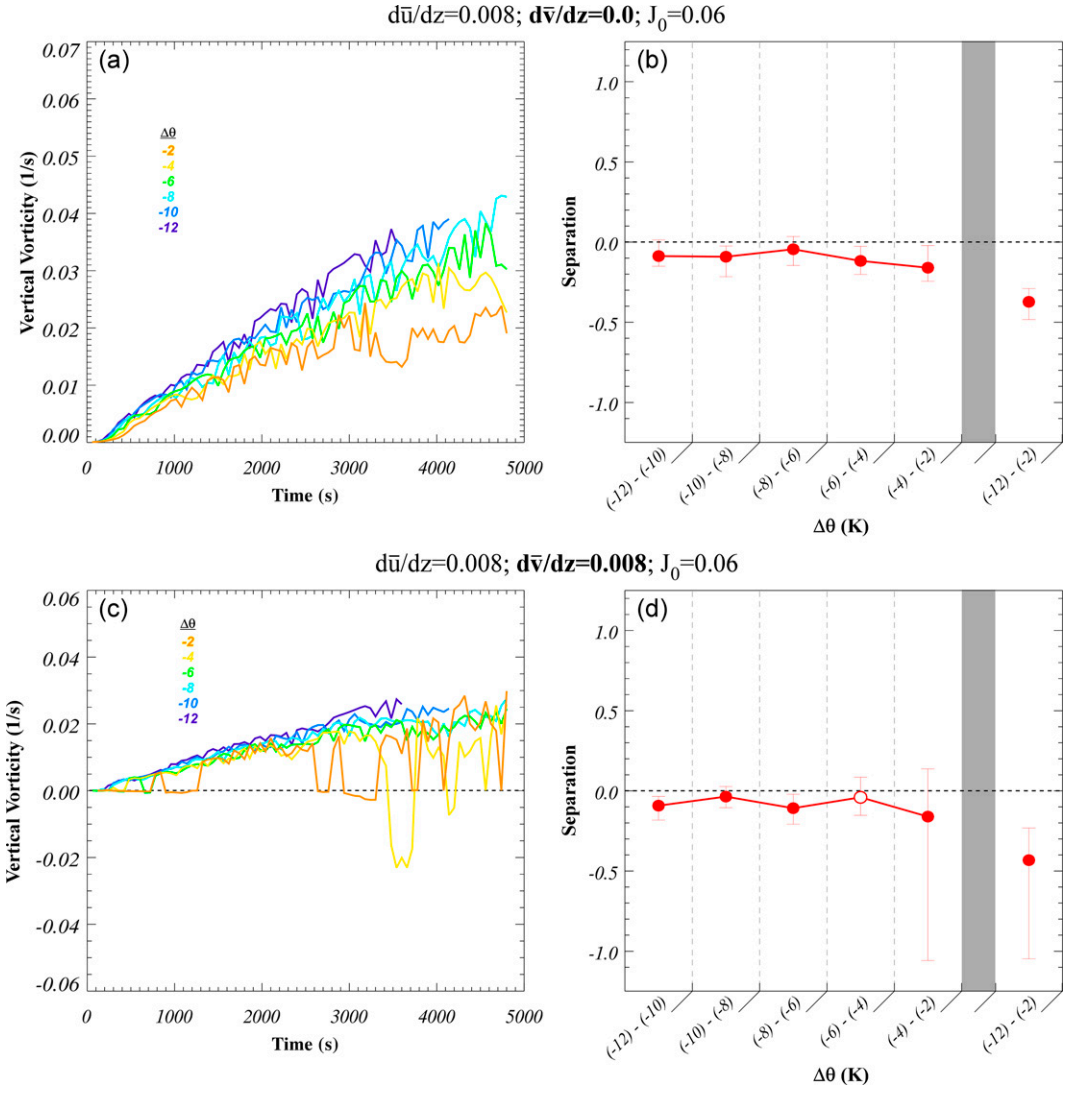

FIG. 21. Maximum ζ_{ns} for the $\Delta\theta$ experiment set for $d\bar{u}/dz = 0.008\,s^{-1}$, $J_0 = 0.06$ K s^{-1}, and (a),(b) $d\bar{v}/dz = 0\,s^{-1}$ and (c),(d) $d\bar{v}/dz = 0.008\,s^{-1}$. (left) Time series and (right) median separations [calculated using (3)] across all times along with the interquartile range illustrated with "whiskers." Filled circles in (b) represent separations that are statistically significant. Separation between experiments with the largest and smallest $\Delta\theta$ are plotted in the rightmost column in (b).

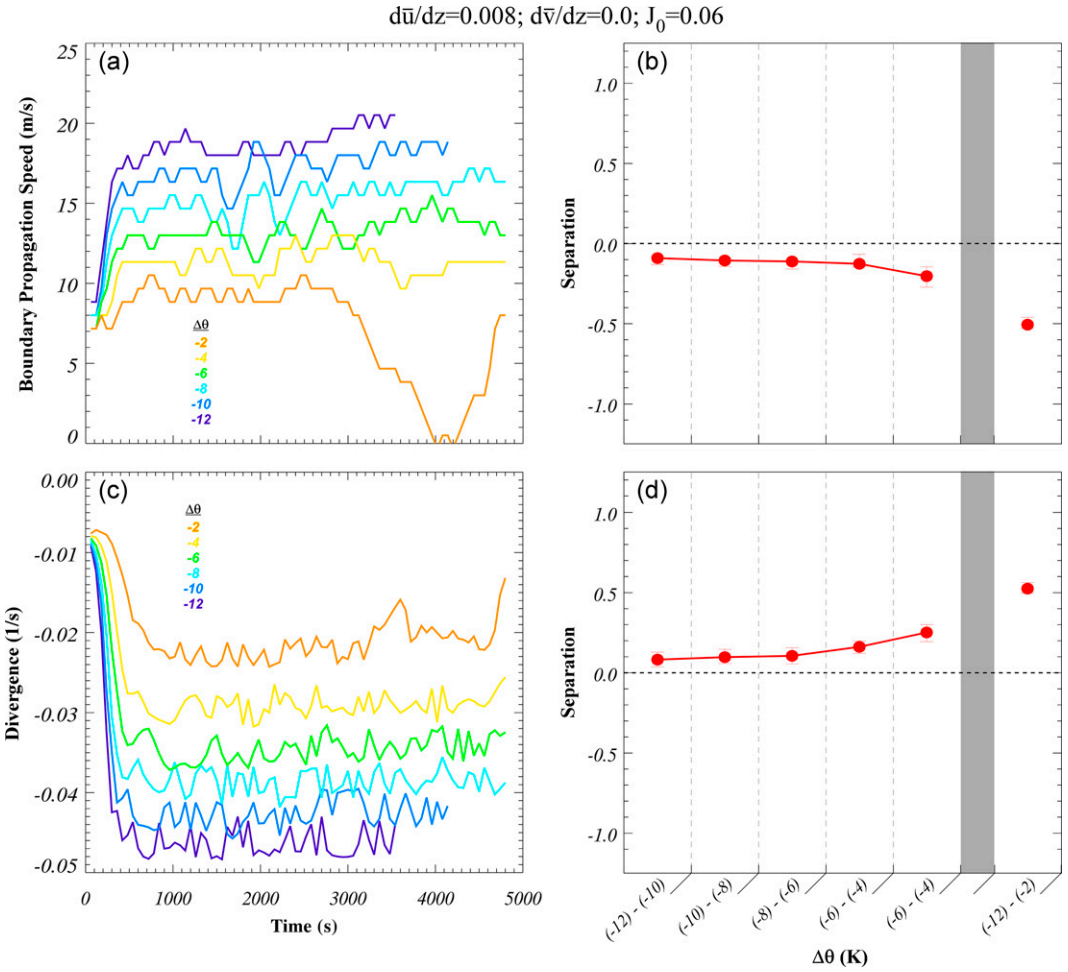

FIG. 22. As in Fig. 21, but for (a),(b) boundary propagation speed and (c),(d) near-surface minimum divergence.

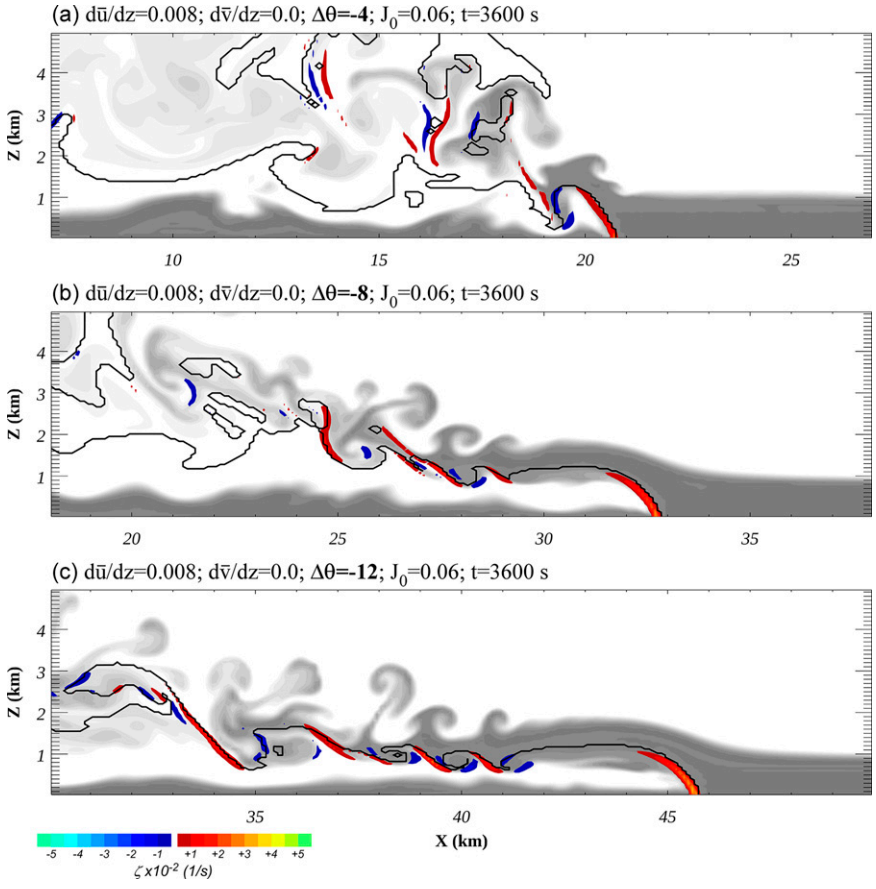

FIG. 23. The ζ_{ns} (shaded in color), tracer concentration (shaded in grayscale), and $\theta' = -1$ K (black contour) at 3600 s for the simulations with $d\bar{u}/dz = 0.008\,s^{-1}$, $d\bar{v}/dz = 0\,s^{-1}$, $J_0 = 0.06$ K s^{-1}, and (a) $\Delta\theta = -4$ K, (b) $\Delta\theta = -8$ K, and (c) $\Delta\theta = -12$ K.

outflow boundaries given the higher potential for evaporative cooling.

Acknowledgments. This work was supported by National Science Foundation Grants OIA-1539070 and IIS-1527113. The authors are very grateful for the careful and constructive reviews of three anonymous reviewers.

Data availability statement. Simulation data used for the analysis presented in this article have been archived in the University of Nebraska–Lincoln's Holland Computing Center's Attic system. These data are available via request made to the corresponding author.

REFERENCES

Atkins, N. T., and M. St. Laurent, 2009: Bow echo mesovortices. Part II: Their genesis. *Mon. Wea. Rev.*, **137**, 1514–1532, https://doi.org/10.1175/2008MWR2650.1.

Brooks, H. E., C. A. Doswell III, and R. B. Wilhelmson, 1994: The role of midtropospheric winds in the evolution and maintenance of low-level mesocyclones. *Mon. Wea. Rev.*, **122**, 126–136, https://doi.org/10.1175/1520-0493(1994)122<0126:TROMWI>2.0.CO;2.

Bryan, G. H., and R. Rotunno, 2014: Gravity currents in confined channels with environmental shear. *J. Atmos. Sci.*, **71**, 1121–1142, https://doi.org/10.1175/JAS-D-13-0157.1.

Chen, C., 1995: Numerical simulations of gravity currents in uniform shear flows. *Mon. Wea. Rev.*, **123**, 3240–3253, https://doi.org/10.1175/1520-0493(1995)123<3240:NSOGCI>2.0.CO;2.

Dahl, J. M. L., M. D. Parker, and L. J. Wicker, 2014: Imported and storm-generated near-ground vertical vorticity in a simulated supercell. *J. Atmos. Sci.*, **71**, 3027–3051, https://doi.org/10.1175/JAS-D-13-0123.1.

Davies-Jones, R. P., 1984: Streamwise vorticity: The origin of updraft rotation in supercell storms. *J. Atmos. Sci.*, **41**, 2991–3006, https://doi.org/10.1175/1520-0469(1984)041<2991:SVTOOU>2.0.CO;2.

——, 2000: Can the hook echo instigate tornadogenesis barotropically? Preprints, *20th Conf. on Severe Local Storms*, Orlando, FL, Amer. Meteor. Soc., 8.3, https://ams.confex.com/ams/Sept2000/webprogram/Paper16085.html.

——, 2015: A review of supercell and tornado dynamics. *Atmos. Res.*, **158–159**, 274–291, https://doi.org/10.1016/j.atmosres.2014.04.007.

——, and H. E. Brooks, 1993: Mesocyclogenesis from a theoretical perspective. *The Tornado: Its Structure, Dynamics, Prediction, and Hazards, Geophys. Monogr.*, Vol. 79, Amer. Geophys. Union, 105–114, https://doi.org/10.1029/GM079.

——, R. J. Trapp, and H. B. Bluestein, 2001: Tornadoes and tornadic storms. *Severe Convective Storms, Meteor. Monogr.*, No. 50, Amer. Meteor. Soc., 167–221.

Droegemeier, K. K., and R. B. Wilhelmson, 1987: Numerical simulation of thunderstorm outflow dynamics. Part I: Outflow sensitivity experiments and turbulence dynamics. *J. Atmos. Sci.*, **44**, 1180–1210, https://doi.org/10.1175/1520-0469(1987)044<1180:NSOTOD>2.0.CO;2.

Fovell, R. G., and Y. Ogura, 1989: Effect of vertical wind shear on numerically simulated multicell storm structure. *J. Atmos. Sci.*, **46**, 3144–3176, https://doi.org/10.1175/1520-0469(1989)046<3144:EOVWSO>2.0.CO;2.

——, and P. S. Dailey, 1995: The temporal behavior of numerically simulated multicell-type storms. Part I: Modes of behavior. *J. Atmos. Sci.*, **52**, 2073–2095, https://doi.org/10.1175/1520-0469(1995)052<2073:TTBONS>2.0.CO;2.

Houston, A. L., 2016: The sensitivity of deep ascent of cold-pool air to vertical shear and cold-pool buoyancy. *Electron. J. Severe Storms Meteor.*, **11** (3), https://ejssm.org/archives/wp-content/uploads/2021/09/vol11-3.pdf.

——, 2017: The possible role of density current dynamics in the generation of low-level vertical vorticity in supercells. *J. Atmos. Sci.*, **74**, 3191–3208, https://doi.org/10.1175/JAS-D-16-0227.1.

——, and D. Niyogi, 2007: The sensitivity of convective initiation to the lapse rate of the active cloud-bearing layer. *Mon. Wea. Rev.*, **135**, 3013–3032, https://doi.org/10.1175/MWR3449.1.

——, and R. B. Wilhelmson, 2011: The dependence of storm longevity on the pattern of deep convection initiation in a low-shear environment. *Mon. Wea. Rev.*, **139**, 3125–3138, https://doi.org/10.1175/MWR-D-10-05036.1.

——, and ——, 2012: The impact of airmass boundaries on the propagation of deep convection: A modeling-based study in a high-CAPE, low-shear environment. *Mon. Wea. Rev.*, **140**, 167–183, https://doi.org/10.1175/MWR-D-10-05033.1.

Klemp, J. B., and R. B. Wilhelmson, 1978: The simulation of three-dimensional convective storm dynamics. *J. Atmos. Sci.*, **35**, 1070–1096, https://doi.org/10.1175/1520-0469(1978)035<1070:TSOTDC>2.0.CO;2.

Laflin, J. M., and A. L. Houston, 2012: A modeling study of supercell development in the presence of a preexisting airmass boundary. *Electron. J. Severe Storms Meteor.*, **7** (1), https://ejssm.org/archives/wp-content/uploads/2021/09/vol7-1.pdf.

Lee, B. D., and R. B. Wilhelmson, 1997: The numerical simulation of non-supercell tornadogenesis. Part I: Initiation and evolution of pretornadic misocyclone circulations along a dry outflow boundary. *J. Atmos. Sci.*, **54**, 32–60, https://doi.org/10.1175/1520-0469(1997)054<0032:TNSONS>2.0.CO;2.

Liu, C., and M. W. Moncrieff, 1996: A numerical study of the effects of ambient flow and shear on density currents. *Mon. Wea. Rev.*, **124**, 2282–2303, https://doi.org/10.1175/1520-0493(1996)124<2282:ANSOTE>2.0.CO;2.

Markowski, P. M., 2016: An idealized numerical simulation investigation of the effects of surface drag on the development of near-surface vertical vorticity in supercell thunderstorms. *J. Atmos. Sci.*, **73**, 4349–4385, https://doi.org/10.1175/JAS-D-16-0150.1.

——, and Y. P. Richardson, 2014: The influence of environmental low-level shear and cold pools on tornadogenesis: Insights from idealized simulations. *J. Atmos. Sci.*, **71**, 243–275, https://doi.org/10.1175/JAS-D-13-0159.1.

——, E. N. Rasmussen, J. Straka, R. Davies-Jones, Y. Richardson, and R. J. Trapp, 2008: Vortex lines within low-level mesocyclones obtained from pseudo-dual-Doppler radar observations. *Mon. Wea. Rev.*, **136**, 3513–3535, https://doi.org/10.1175/2008MWR2315.1.

——, Y. Richardson, and G. Bryan, 2014: The origins of vortex sheets in a simulated supercell thunderstorm. *Mon. Wea. Rev.*, **142**, 3944–3954, https://doi.org/10.1175/MWR-D-14-00162.1.

Rotunno, R., and J. B. Klemp, 1982: The influence of the shear-induced pressure gradient on thunderstorm motion. *Mon. Wea. Rev.*, **110**, 136–151, https://doi.org/10.1175/1520-0493(1982)110<0136:TIOTSI>2.0.CO;2.

——, ——, and M. L. Weisman, 1988: A theory for strong, long-lived squall lines. *J. Atmos. Sci.*, **45**, 463–485, https://doi.org/10.1175/1520-0469(1988)045<0463:ATFSLL>2.0.CO;2.

Schenkman, A. D., M. Xue, and A. Shapiro, 2012: Tornadogenesis in a simulated mesovortex within a mesoscale convective system. *J. Atmos. Sci.*, **69**, 3372–3390, https://doi.org/10.1175/JAS-D-12-038.1.

Thuburn, J., 1995: Dissipation and cascades to small scales in numerical models using a shape-preserving advection scheme. *Mon. Wea. Rev.*, **123**, 1888–1903, https://doi.org/10.1175/1520-0493(1995)123<1888:DACTSS>2.0.CO;2.

Trapp, R. J., and M. L. Weisman, 2003: Low-level mesovortices within squall lines and bow echoes. Part II: Their genesis and implications. *Mon. Wea. Rev.*, **131**, 2804–2823, https://doi.org/10.1175/1520-0493(2003)131<2804:LMWSLA>2.0.CO;2.

Walko, R. L., 1993: Tornado spin-up beneath a convective cell: Required basic structure of the near-field boundary layer winds. *The Tornado: Its Structure, Dynamics, Prediction, and Hazards*, *Geophys. Monogr.*, Vol. 79, Amer. Geophys. Union, 89–95.

Wheatley, D. M., and R. J. Trapp, 2008: The effect of mesoscale heterogeneity on the genesis and structure of mesovortices within quasi-linear convective systems. *Mon. Wea. Rev.*, **136**, 4220–4241, https://doi.org/10.1175/2008MWR2294.1.

Xu, Q., 1992: Density currents in shear flows—A two-fluid model. *J. Atmos. Sci.*, **49**, 511–524, https://doi.org/10.1175/1520-0469(1992)049<0511:DCISFA>2.0.CO;2.

Xue, M., Q. Xu, and K. K. Droegemeier, 1997: A theoretical and numerical study of density currents in nonconstant shear flows. *J. Atmos. Sci.*, **54**, 1998–2019, https://doi.org/10.1175/1520-0469(1997)054<1998:ATANSO>2.0.CO;2.